Transparent and Flexible $Mn_{1-x-y}(Ce_xLa_y)O_{2-\delta}$ Ultrathin-Film Device for Highly-Stable Pseudocapacitance Application

Samane Maroufi[1], Rasoul Khayyam Nekouei[1§], Sajjad S. Mofarah[1§], Anthony P. O'Mullane[2], and Veena Sahajwalla[1]*

[1] Centre for Sustainable Materials Research and Technology, SMaRT@UNSW, School of Materials Science and Engineering, UNSW Sydney, NSW 2052, Australia
[2] School of Chemistry and Physics, Queensland University of Technology (QUT), Brisbane, QLD 4001, Australia
*Corresponding author, Email: s.maroufi@unsw.edu.au
§ Authors have equal contributions.

Abstract

Control over fabrication of state-of-the-art portable pseudocapacitors with desired transparency, mechanical flexibility, capacitance, and durability has shown to be challenging with fundamental implications. Here defect-rich $Mn_{1-x-y}(Ce_xLa_y)O_{2-\delta}$ ultrathin films with controllable thicknesses (5-650 nm) and transmittance (~29-100 %) are fabricated using the electrochemical chronoamperometric technique. According to the percolation impacts on the optoelectronic properties of the ultrathin films, a representative $Mn_{1-x-y}(Ce_xLa_y)O_{2-\delta}$ film with 86% transmittance exhibits an outstanding areal capacitance of 3.4 $mF{\cdot}cm^{-2}$, which is revealed to be mainly attributed to the intercalation/de-intercalation of anionic O^{2-} charge carriers through the atomic tunnels of the stratified $Mn_{1-x-y}(Ce_xLa_y)O_{2-\delta}$ crystallites. Further, the $Mn_{1-x-y}(Ce_xLa_y)O_{2-\delta}$ exhibits excellent capacitance retention of ~90% after 16,000 cycles. Such stability is shown to associate with intervalence charge transfers occurring among interstitial Ce/La cations and Mn oxidation states within the $Mn_{1-x-y}(Ce_xLa_y)O_{2-\delta}$ structure, which retain Mn^{2+} and Mn^{3+} at high densities over the charge/discharge process. The energy and power densities of the transparent flexible $Mn_{1-x-y}(Ce_xLa_y)O_{2-\delta}$ full-cell pseudocapacitor device, with solid-state electrolyte, is measured to be 0.088 $\mu Wh.cm^{-2}$ and 843 $\mu W.cm^{-2}$, respectively. These values show insignificant changes under vigorous twisting and bending to 45˚, 90˚, and 180˚ confirming these materials are intriguing alternatives for size-sensitive energy storage devices.

1. Introduction

Transparent and flexible energy storage devices are critical components in portable power-integrated electronic systems[1,2] such as shape-conformable sensors, flexible displays, capacitive touch screens, and solar cells[3–6]. Compared to other energy storage devices, pseudo and supercapacitors are known as ideal candidates for implementing such flexible and transparent characteristics due to their multifunctional properties and excellent features, including high-power density, fast charge/discharge rate, and long cycling life[7]. Conductivity, mechanical flexibility, transparency, electrochemical capacitance, and durability of the used materials determine the performance of such energy storage devices[7]. To meet these criteria, candidate materials need to be designed into two-dimensional architecture. To date, several examples of flexible and transparent capacitors have been reported[7] which can be classified into the following subgroups: **I.** uniform ultrathin-films fabricated from a range of materials such as graphene[8–13], MXene[14,15] (namely two-dimensional transition metal carbides, nitrides, or carbonitrides), conductive polymers[4,16–19], transition metal oxides such as MnO_2[20], NiO[21,22] Co_3O_4[7], RuO_2[23], and WO_3[24], **II.** 1D nanomaterials interlaced films from CNTs[25,26] and metal nanowires[13,27,28], **III.** irregular mesh-like films[29], **IV.** orderly patterned films[3,30–34], and **V.** interdigitated patterned films[35–38].

Among these, uniform ultrathin-films hold greater promise due to being highly stable at severe twisting, strongly adherent to the surface, and cost-effective for high-yield fabrication[39–42]. Further, transition metal oxides (TMOs), by far, exhibit superior energy density relative to those of carbon-based materials. This is owing to their intrinsic high theoretical capacitances, multivalence oxidation states, and rapid redox reactions. Nonetheless, reproducible fabrication of these materials with controllable thickness, their intrinsic low conductivity, and poor cycling stability limit their widespread uses in flexible and size-sensitive pseudocapacitance applications. One of the promising approaches to overcome such shortcoming is engineering bandgap alignment to improve ionic and electronic conductivities by formation of substitution or interstitial atomic defects using extrinsic ions[4].

Here we demonstrate an electrochemical-based synthesis method to fabricate defect-rich ultrathin $Mn_{1-x-y}(Ce_xLa_y)O_{2-\delta}$ films of tailored thicknesses. The as-synthesised films, which is derived from electronic waste (e-waste, *i.e.*, end-of-life nickel-metal hybrid batteries) precursors, were made of atomically thin nanosheets and exhibited high mechanical flexibility, transparency, and large density of mixed oxidations states. The electrochemical performance of the films showed promising areal and gravimetric capacitances and exceptional long-term cycling stability. The energy and power densities of the $Mn_{1-x-y}(Ce_xLa_y)O_{2-\delta}$

symmetric pseudocapacitor device were also measured to 0.088 μWh cm^{-2} and 843 μW cm^{-2}, respectively, which remained unchanged after vigorous bending and twisting. The present work enlarges application of flexible defect-rich TMO-based pseudocapacitor for transparent portable electronic devices, where superior durability can be obtained through controllable design of architecture and structure.

2. Results and Discussion

Synthesis and characterisation of defect-rich $Mn_{1-x-y}(Ce_xLa_y)O_{2-\delta}$ ultrathin films. The fabrication of ultrathin films involves selective electrodeposition of dissolved cationic species using a *polarisation-based anodic chronoamperometric technique* in an aqueous electrolyte. The electrolyte, which was obtained by e-waste recovery process, consisted of Ce^{3+}, Mn^{2+} and La^{3+} ions (**Table S1**, Supporting Information). To obtain the optimum voltage for film deposition, where co-oxidation of Ce^{3+} and Mn^{2+} ions occur, cyclic voltammetry (CV) analysis was carried out within a potential range of 0.0-1.0 V vs SCE (0.38-1.38 V vs. RHE) at pH of 2.5. The resulting cyclic voltammogram (blue curve) is shown in **Figure 1**a, where the increase in anodic current with a shoulder at 0.92 V and a well-defined reduction peak at 0.72 V are attributed to the $Mn^{2+} \leftrightarrow Mn^{4+}$ reactions.

Thermodynamic calculations of the $Ce^{3+} \rightarrow Ce^{4+}$ oxidation reaction using speciation and Pourbaix diagrams revealed that the formation of CeO_2 may occur at potentials ~0.6 V vs. SCE. This is verified with the experimental CV results (red voltammogram in **Figure 1**a). The current density, which is an indication of the mass deposition, for Ce^{3+} oxidation is in the order of μA, much lower than that for Mn^{2+} oxidation (mA), suggesting that the MnO-based structure is the main phase deposited. Further, the water oxidation reaction, which is E_{H_2O/O_2}=1.23 V vs. RHE, should be avoided and therefore the optimum voltage for synthesis of MnO_{2-x} (oxidation of aqueous Mn^{2+}) was found to be 0.92 V vs. SCE (1.3 V vs. RHE).

Although anodic deposition requires direct oxidation through a faradic process, a high concentration of La^{3+} (~72 times more than Mn^{2+} and ~8 times more than Ce^{3+}) present in the electrolyte can cause entrapment of La^{3+} in the as-crystallised $Mn_{1-x}(Ce_x)O_{2-\delta}$, during the co-oxidation of Ce^{3+} and Mn^{2+}. Despite the presence of Ni and Nd in the electrolyte precursor, the time-of-flight secondary ion mass spectroscopy's (TOF-SIMS) depth profile of the film (**Figure S1**a, Supporting Information) reveals no deposition of these two elements. The depth profile of atomic concentrations of the elements obtained by X-ray photoelectron spectrometer (XPS) is shown in **Figure S1**b, Supporting Information, where the concentrations of Mn, Ce, La, O are measured to be 45.6-46.9, 3.2-3.8, 2.8-3.2, and 46.4-47.8 at%, respectively.

The chemical structure of the ultrathin film was characterised using Raman microspectra, the data of which is shown in **Figure S2**, Supporting Information. The three predominant bands in pink colour centred at 504, 568, and 639 cm^{-1} are related to Mn-O in-plane/out-of-plane stretching vibration of δ-MnO_2[43,44]. The deconvoluted bands (blue) positioned at 386, 580, 649 and the band (orange) at 723 cm^{-1} are assigned to vibrational modes of E_1 and A_{2g} corresponding to α- and β- phases of MnO_2, respectively[45,46]. The mode at 606 cm^{-1} is associated with Mn-O stretching vibrations of Mn_2O_3[47], which is only present for the $Mn_{1-x-y}(Ce_xLa_y)O_{2-\delta}$ structure. The Raman characteristic peaks associated with CeO_2 and La_2O_3 structures were not found. Nonetheless, comparing the Raman spectrum of pristine MnO_{2-x} with that of the $Mn_{1-x-y}(Ce_xLa_y)O_{2-\delta}$, shown in **Figure S2**, Supporting Information, partial phase transformation of δ-MnO_2 to α- and β- phases can be owing to the presence of La^{3+} and Ce^{3+}.

According to Hume-Rothery's rule for substantial solid solubility, the large ionic size mismatches of 74% and 65% for La^{3+}, with an ionic radius of 0.1172 nm, and Ce^{4+}, with an ionic radius of 0.111 nm, respectively, suggests that the formation of a solid solution through a substitutional mechanism is highly unlikely. Therefore, this leaves only one possibility, which is interstitial solid solubility of the rare earth cations (REC) in the MnO_2 structure. The latter theory can be rationalised according to the types of MnO_2 crystal structures, which are schematically illustrated in **Figure 1**b. δ-MnO_2 has 2D layered structure (1×∞) with an interlayer separation of ~7 Å[48,49]. Such a large interlayer gap can easily accommodate the large-size RECs with partial phase transformation and minimal distortion[50]. The RECs can also stabilise the (1×∞) tunnels and thus shift the phase into α/β-MnO_2. In addition, α-MnO_2 provides atomic tunnels along the [001] direction (c-axis)[51] with the lateral dimensions of 2×2 (4.6×4.6 Å) and 1×1 (1.9×1.9 Å)[52]. The atomic tunnels along the $[1\bar{1}0]$ direction of β-MnO_2 posses the lateral dimensions of 3.4×3.4 Å. Therefore, similar to δ-MnO_2, the interstitial introduction of RECs is likely to occur in α/β-MnO_2 during crystallisation, as has previously been reported[53]. The interstitial solubility of REC in MnO_2 is also expected to form high concentrations of structural defects.

To investigate the chemistry of structural defects that originate from unpaired electrons, electron paramagnetic resonance (EPR) analysis was conducted. The resultant spectra for pristine MnO_{2-x} and $Mn_{1-x-y}(Ce_xLa_y)O_{2-\delta}$ are shown in **Figure 1**c. As for Mn ions, Mn^{2+} ($3d^5$, S=5/2) and Mn^{4+} ($3d^3$, S=3/2) are EPR active, while Mn^{3+} ($3d^4$, S=2), with no unpaired electrons, is EPR inactive. For pristine MnO_{2-x}, the EPR signal reveals a single broad line of Gaussian-like shape with a broad linewidth (ΔH_B=367 mT) owing to the dipole-dipole exchange interactions between two identical paramagnetic Mn^{4+} ions. The *g* factor of the

signal was measured to be 1.96±0.01, which is consistent with those reported for MnO_2 nanostructures. For the $Mn_{1-x-y}(Ce_xLa_y)O_{2-\delta}$ film, the corresponding EPR signal shows multiple hyperfine splitting at magnetic fields in the range of 320-380 mT that can be ascribed to the interactions between Mn^{2+}, Ce^{3+}, and La^{3+}. The co-existence of Mn^{4+} and Mn^{2+} for MnO and MnO_2 is manifested in the form of sharp hyperfine features, with the *g* values[54] of 2.16, 2.10, and 1.96, with shoulders (rounded humps) on each hyperfine, respectively. The presence of Mn^{2+} is further justified by revealing the hyperfine feature with a *g* value of 2.005 associated with the Mn_3O_4 ($2MnO{\cdot}MnO_2$) phase in the system[55]. It is significant to note that the hyperfine interaction between unpaired electrons and atom nuclei yields information regarding the identity of ions and their distances. Ce has four stable isotopes (^{136}Ce, ^{138}Ce, ^{140}Ce, and ^{142}Ce) and two valences, 3+ and 4+, with respective electron configurations of $4f^1$ and $5p^6$. Despite the filled *d* orbital with the potential of forming ten absorption peaks, Ce^{4+} has no unpaired electrons and consequently is EPR-inactive. In contrast, Ce^{3+} has a single unpaired electron (EPR-active). **Table S2** Supporting Information, provides *g* factors obtained according to the hyperfine interactions. As for the Ce dopant, the presence of Ce^{3+}, O_2^-, and Ce^{3+}–O^-–Ce^{4+} were identified as shown in **Figure 1**c. The hyperfine feature positioned at g=2.016 indicates the existence of superficial isolated anionic vacancies caused by superoxide ligands linking to coordination Ce^{4+} ions [54]. Furthermore, the EPR hyperfine feature at g=2.12 is correlated to the isolated vacancies formed by superoxide ions in Ce^{4+}-O_2^- species[54]. These types of isolated vacancies are resistant to decomposition and thus further electron transfer can occur from the sample surface. In addition, the hyperfine feature with a *g* value of 1.96 can be assigned to a Ce^{3+}-$V_{\ddot{O}}$-Ce^{4+} interaction as a reflection of anionic vacancies on the surface

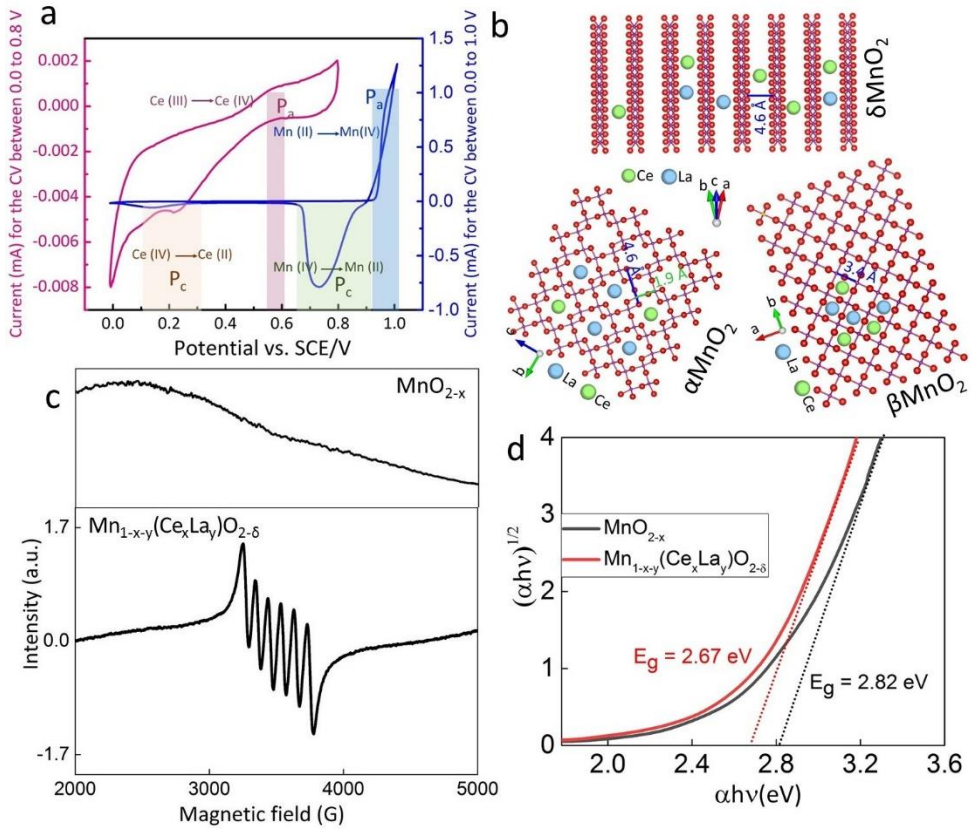

Figure 1. a) Cyclic voltammograms (CVs) of the precursor using a three-electrode configuration with FTO electrode as working electrode (WE), spiral Pt wire as counter electrode (CE), and standard calomel electrode (SCE) as reference electrode (RE), at 10 $mV.s^{-1}$ scan rate and 70°C, b) crystal structure of δ-, α- and β-MnO_2 loaded with La^{3+} and $Ce^{3+/4+}$, c) electron paramagnetic resonance (EPR) signals *vs*. magnetic field curve of MnO_{2-x} and $Mn_{1-x-y}(Ce_xLa_y)O_{2-\delta}$ samples, and d) Tauc plot (UV-visible $(\alpha hv)^{1/2}$ *vs*. E_P curve) for pristine MnO_{2-x} and $Mn_{1-x-y}(Ce_xLa_y)O_{2-\delta}$ powder samples.

Interstitial diffusion of Ce and La cations into the lattice structure can potentially modify the physical and chemical properties of functional materials, by controlling their ionic and electronic conductivities[56]. The atomic insertion into the MnO_{2-x} crystal structure as cation intercalation can change the bonding energy via producing new molecular orbits which introduces impurity levels in semiconductors that can reduce the

bandgap of the material[57]. The bandgap was evaluated via UV-Vis absorption spectroscopy for $Mn_{1-x-y}(Ce_xLa_y)O_{2-\delta}$ and pristine MnO_{2-x} film electrodes, with similar thicknesses. Tauc plots in **Figure 1**d show that the bandgap shortened from 2.57 to 2.41 eV as a result of Ce and La co-insertion. Accordingly, the concentration of free movable electrons increases, which enhances electric conductivity. The substantial point defects and oxygen vacancies in the structure of MnO_{2-x} can also contribute to improvement of electric conductivity[50]. This enhancement in electrical conductivity resulting from bandgap tuning and oxygen vacancies will in principle further improve the electrochemical performance, which is normally limited by carrier concentration and mobility[57].

Optical and chemical analysis of transparent ultrathin films. The flexibility of the anodic chronoamperometric synthesis allows for the fabrication of ultrathin films with tailored thicknesses and thereby transparency. **Figure 2**a shows camera images of $Mn_{1-x-y}(Ce_xLa_y)O_{2-\delta}$ ultrathin films where the film thickness increases from left to right as evident by diminution of their transparencies. The morphological alteration of the ultrathin films as a function of deposition time was explored using field-emission scanning electron microscopy (FE-SEM) images, as shown in **Figure 2**b. The sequential FE-SEM images reveal that ultrathin films are deposited through stacking of the extremely thin nanoflakes across the surface of the fluorine-doped tin oxide (FTO) substrate. **Figure 2**c shows the transmittance spectrum obtained for each film within a wide range between 300 and 900 nm. The relationship between the optical transmittance (T%) of the films, at 550 nm, and thicknesses is plotted, as shown in **Figure 2**d. The results show that for thicknesses <46 nm (samples II, III, IV), outstanding T% value of >~90% can be achieved. However, increasing the thickness to 78 nm (sample V) results in a considerable T% reduction to <60%. Furthermore, an increase in thickness to 627 nm yields a low T% value of 14% (sample VIII). **Table S3**, Supporting Information, summarises the physical and optical properties of the ultrathin films.

To measure the thickness of the films, TOF-SIMS analysis was used. The results of two-dimensional (2D) TOF-SIMS analysis for three representative samples II, III, and IV are shown in **Figure 2**e. According to the penetration depth of the ion beam, the thickness of the films were measured to be 11, 28, and 46 nm for samples II, III, and IV, respectively. **Figure 2**e shows bulk distribution of Mn, Ce, and La ions for the three representative samples II, III, and IV revealing a homogenous distribution of the ions across the ultrathin films.

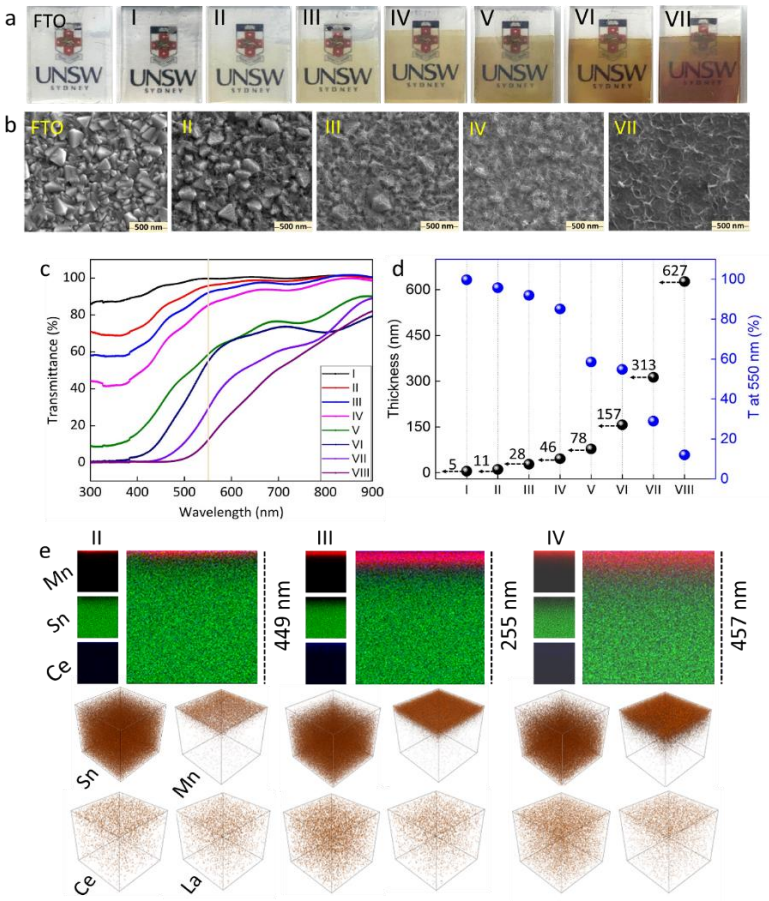

Figure 2. a) Optical images of the as-synthesised $Mn_{1-x-y}(Ce_xLa_y)O_{2-\delta}$ thin-film electrodes, b) FE-SEM images of the surface of selected samples presented in (a), c) UV-Vis transmittance spectra of the corresponding films in the visible region, d) transmittance of the films at the wavelength of 550 nm as a function of thickness; and e) 2D and 3D TOF-SIMS elemental images for the measurement of the thickness, qualitative concentration, and distribution of elements in the as-synthesised films.

Electrochemical performance of ultrathin films. The electrochemical behaviour of the $Mn_{1-x-y}(Ce_xLa_y)O_{2-\delta}$ ultrathin films were investigated in a three-electrode configuration system in a 2 M KOH electrolyte. **Figure 3**a, b shows voltammograms of the films at scan rates of 5 and 50 $mV{\cdot}s^{-1}$ within the potential window of -0.3 to 0.5 V vs SCE. The peak areas of the voltammograms, which is associated with the areal capacitance ($F{\cdot}cm^{-2}$) of the films, are shown to be enhanced by increasing the film thickness. The difference in the cyclic voltammogram shapes obtained at 5 and 50 $mV{\cdot}s^{-1}$ is ascribed to the alteration of charge/discharge mechanism and the depletion of charge carriers as a result of the rapid kinetics of the charge/discharge process. It is critical to note that the insignificant contribution of the substrate for the thinnest film, *i.e.*, 11 nm, # II, was measured to be only ~3%, as shown in **Figure S3**c, Supporting Information. Further analysis of the electrochemical behaviour of the films was carried out using cyclic voltammetry over a wide range of scan rates. The details of the results are shown in **Figure S4**a-c, Supporting Information. Furthermore, a comparative plot of areal and gravimetric capacitances against the films' thicknesses, at two scan rates of 5 and 50 $mV{\cdot}s^{-1}$, is shown in **Figure 3**c. The results reveal that increasing the film thickness from 10 to 600 nm reduced the gravimetric capacitance by 53%, while the areal capacitance increased from ~0.1 $mF.cm^{-2}$ to 32.0 $mF.cm^{-2}$. The apparent capacitance gap between the scan rates originates from the contribution of diffusion, which becomes insignificant at a rapid scan rate of 50 $mV{\cdot}s^{-1}$.

To confirm the results of capacitance obtained by cyclic voltammetry, the galvanostatic charge/discharge (GCD) technique was used. **Figure 3**d shows a plot of areal capacitance against current density, which are consistent with those obtained from the CV technique. The other gravimetric and areal capacitances of the ultrathin films at different scan rates and current densities are illustrated in **Figure S4**g-i, Supporting Information, respectively.

Electrochemical impedance spectroscopy (EIS) of the films, recorded at open circuit potential (OCP) with a potential amplitude of 10 mV, is shown in **Figure 3**e. To analyse the EIS measurements, a physicochemical transport model was applied (shown in the inset of **Figure 3e**), where the electrode resistance (R_p) is obtained by summation of resistances in the bulk electrode and at the interface between the electrode and current collector[58]. The R_p values for the combination of FTO substrate and films #II, #III, and #IV were measured to be ~9.5, 10.5, and 13.0 Ω, respectively. The calculated results for the $Mn_{1-x-y}(Ce_xLa_y)O_{2-\delta}$ film indicates that with ~17 nm increase in the thickness, the resistance escalates by 1.0-1.5 Ω. Furthermore, the sum of the charge and mass transfer resistance ($R_{ct} + R_{mt}$) was measured to be ~0.29, ~0.65, and ~0.94 Ω for the films #II, #III, and #IV, respectively. The transition from medium (semicircle) to low frequencies (linear line), which is represented by a Warburg diffusion element (W_d), describes the diffusion of ions in the electrolyte[59]. The slope of the line, at low frequencies, indicates whether the charging is under EDL formation (>45°) or limited by ion diffusion in the electrolyte (<45°e)[58]. The general sharp slopes achieved for all the samples indicates the presence of the EDL layer and predominant contribution of pseudocapacitance[59].

The capacitance retention of the $Mn_{1-x-y}(Ce_xLa_y)O_{2-\delta}$ films #II, #III, and #IV, and pristine MnO_{2-x} film (with the thickness equal to #IV, *i.e.*, 46 nm) were investigated using GCD analysis at current densities of 35, 20, and 15 A cm^{-1}, respectively. **Figure 3**f shows excellent electrochemical stability with 95, 90, and 93% capacitance retention for films #II, #III, and #IV, respectively, after 16000 charge/discharge cycles. Such outstanding performance stability can be associated with the presence of the REEs cations that are shown to enhance the structural and corrosive stabilities[60]. In contrast, the pristine MnO_{2-x} film suffers from rapid degradation while cycling.

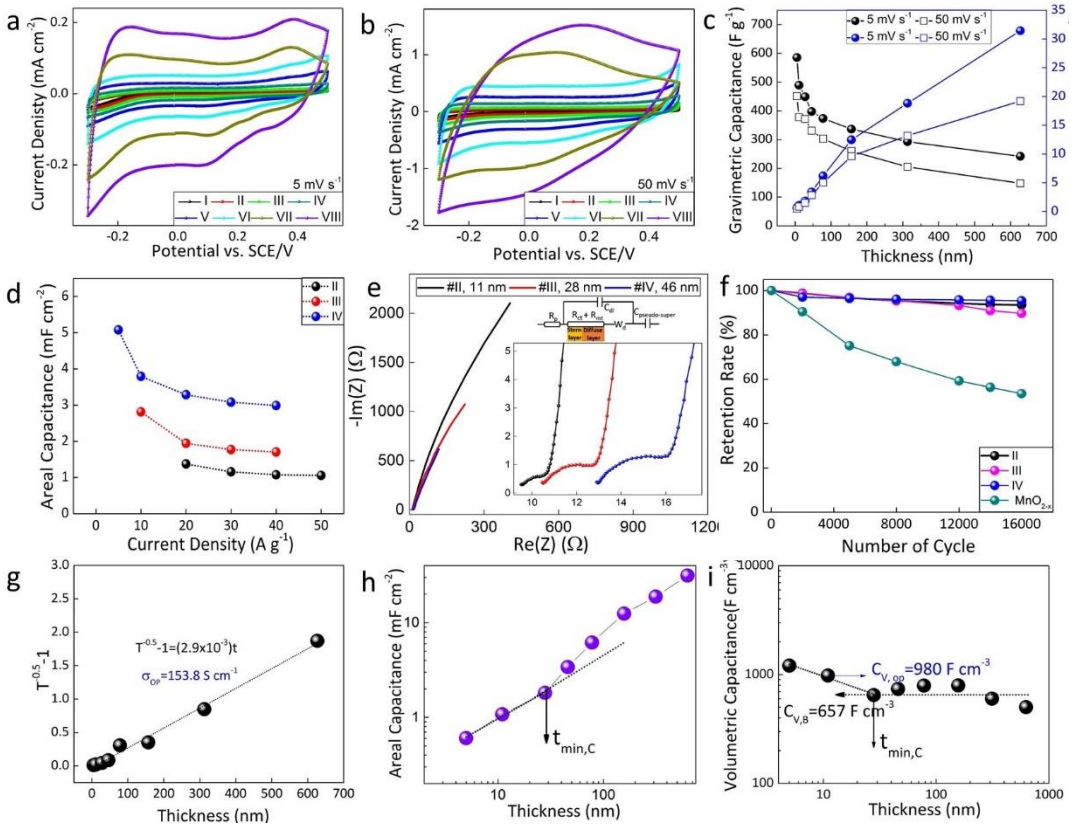

Figure 3. Electrochemical results of the as-synthesised $Mn_{1-A}Ce_xLa_yO_{2-B}$ thin-film electrodes using a three-electrode cell configuration (thin-film electrode as WE, Pt spiral wire as CE, and SCE as RE) in the potential window from -0.3 to 0.5 *vs* SCE/V in a 2 M KOH aqueous solution. CV of electrodes at scan rate of a) 5 $mV.s^{-1}$, and b) 50 $mV.s^{-1}$; c) areal and gravimetric capacitances as a function of film thickness; d) areal capacitance as a function of scan rate for the three thinnest electrodes II, III, and IV based on GCD test; e) EIS for the synthesised electrodes at 0.0 *vs*. SCE/V between 100 kHz to 100 mHz with the potential amplitude of 10 mV; f) stability performance of the three $Mn_{1-x-y}(Ce_xLa_y)O_{2-\delta}$ electrodes #II (at 35 $A.g^{-1}$), #III (at 20 $A.g^{-1}$), and #IV (at 15 A g^{-1}), and pristine MnO_{2-x} film (at 15 $A.g^{-1}$), at 2 M KOH and room temperature. g-i) The impact of percolation and thickness on the optoelectronic properties of ultrathin-films; g) plot of film transmittance expressed as $T^{-0.5}$-1 as a function of film thickness, h) areal capacitance, and i) volumetric capacitance of the films as a function of film thickness, using CV results at scan rate of 5 $mV.s^{-1}$ in a 2 M KOH electrolyte.

To obtain an optimal transparent pseudocapacitor, establishing an equilibrium between the specific capacitance, which is either gravimetric or areal, and optoelectronic properties is critical. In the present work, ultrathin film #II, with a thickness of 11 nm, exhibited a relatively low areal capacitance of 1.37 $mF.cm^{-2}$, but the highest transparency (99%) (**Figure 2**c). The increase in thickness to 28 nm (sample #III) and 46 nm (sample #IV) resulted in enhancement of the areal capacitance to 2.81 and 5.07 mF cm^{-2}; however, reduced the gravimetric capacitance from 720 to 622 $F.g^{-1}$ while limiting the transparency to 80% and 72%, respectively. Although transparency can be achieved via fabrication of ultrathin electrodes, minimising the thickness to increase the transparency (**Figure 2**c) can introduce certain limitations due to percolation pathways, below which the obtained transparency is not efficient for energy storage applications.

As a matter of fact, the intrinsic properties, including optoelectronic properties, are thickness independent[61] only in bulk-like materials[62]. Therefore, the transition from bulk-like to percolative regimes, *i.e.*, ultrathin thicknesses, and percolation impact in ultrathin films, should be taken into account[63]. This is because when the thickness falls below a transition thickness, the percolative impact begins to control the optoelectrical conductivity[14,64,65]. Besides, while volumetric capacitance is thickness invariant for thick films, a significant deviation from the bulk-like behaviour was observed for ultrathin-films.

To demonstrate the presence of both bulk-like and percolative regimes, a further investigation was carried out, where the impact of thickness on the optoelectronic properties of ultrathin-films was analysed. For conductive films, the transmittance (T) for a given thickness, t, is controlled by the optical conductivity (σ_{op}) through Eq. 1[4,19,62]:

$$T = \left[1 + \frac{Z_0 \sigma_{op} t}{2}\right]^{-2} \quad \text{(Eq. 1)}$$

where z_0 is the impedance of free space (377 Ω). Therefore, the optical conductivity (σ_{op}) was calculated to be σ_{op}=153.8 $S \cdot cm^{-1}$ by measuring the slope of the line in the plot of $T^{-1/2}$-1 (at 550 nm) against the thickness of the film (t), as shown in **Figure 3**g. This value is the lowest reported to date for transparent supercapacitors such as SWCNT films (σ_{op}=150-200

S.cm^{-1})[66,67] and graphene films (σ_{op}=100-2000 S cm^{-1})[68].

The areal capacitances that were calculated based on the CV curves are plotted against the film's thickness in **Figure 3**h. As shown, for thin films with thicknesses below 28 nm, the areal capacitance varies linearly with thickness. It is reasonable to consider this thickness value as the transition thickness ($t_{min,C}$=28 nm) around which the regime varies from percolative to bulk-like behaviour.

To further confirm this outcome, the film thickness was used to calculate the volumetric capacitance, which is plotted as a function of thickness as shown in **Figure 3**i. Considering that the as-synthesised film possesses a well-defined surface area per unit volume, then this volumetric capacitance (C_V) should be independent of the film's thickness for a bulk-like film (assuming good electrolyte wetting). In the bulk-like regime ($t_{min,C}$>28 nm), as expected, C_V is relatively constant with a small variation around a mean value of 657 F.cm^{-3}. In contrast, in the percolative region ($t_{min,C}$<28 nm), a significant increase in CV value is observed, which is attributed to the lower thickness, which facilitates and expedites the movement of the electrons towards the current collector substrate which therefore results in higher capacitance.

While the thicknesses can be reduced to increase transmittance, the areal capacitance decreases (**Figure 3**h). Therefore for a trade-off between transmittance and capacitance and in order to optimise the areal capacitance (C_A) at a certain transparency, the "capacitive figure of merit" (FoM_C), C_V/σ_{op}, should be maximised[62]. The FoM_C is determined to be C_V/σ_{op}=7.8, 6.3, and 4.2 F·S^{-1} for electrodes II, III and IV, respectively. The values obtained in the present work are amongst the highest reported to date including a RuO_2/PEDOT:PSS thin film (C_V/σ_{op}=6.1 F·S^{-1})[4], PEDOT:PSS (C_V/σ_{op}=1.7 F·S^{-1})[62], and a disordered SWNT electrode (C_V/σ_{op}=0.3 F·S^{-1})[19].

Impact of REEs in $Mn_{1-x-y}(Ce_xLa_y)O_{2-\delta}$ lattice on energy storage and cycling stability

Energy storage mechanism. There are two principal mechanisms during charge/discharge of the $Mn_{1-x-y}(Ce_xLa_y)O_{2-\delta}$ film: **(i)** redox reactions at the surface of the electrode, which is the characteristic of pseudocapacitance[69–71] and **(ii)** intercalation/de-intercalation of the cations, which is the characteristic of intercalation pseduocapacitance[72,73]. The former mechanism is determined by the number of active sites, *e.g.*, vacancies, at the surface of the electrode, while the latter mechanism requires crystallographic pathways that allow the charge carriers to intercalate/de-intercalate within/out of the bulk of the electrode.

To elucidate the intercalation/de-intercalation mechanism, alterations voltammogram shapes in response to the increasing pH of the electrolyte (*i.e.*, increasing hydroxyl ion (OH^-) concentration) were investigated and hence the resultant CV are shown in **Figure 4**a. With the increase of the OH^- concentration, the peak potentials for both reduction and oxidation reactions shifted to lower values which clarifies the key role of OH^- ions during the charge/discharge process. During the anodic scan, the voltammogram exhibits two distinctive peaks related to two oxidation reactions of $Mn^{2+} \rightarrow Mn^{3+}$ and $Mn^{3+} \rightarrow Mn^{4+}$. It is significant to note that the former oxidation reaction shows greater intensity implying a higher concentration of Mn^{2+}, in consistent with the results of EPR analysis (**Figure 1**c). The large concentration of OH^-, and thus its high accessibility, in the electrolyte would result in the dissociation of OH^- to O^{2-} during the anodic scan[74]. This can be followed by intercalation of the liberated O^{2-} into the vacancy sites and atomic gaps within 2D layered structure (1×∞) of δ-MnO_2 of the $Mn_{1-x-y}(Ce_xLa_y)O_{2-\delta}$ electrode, which is more likely in comparison to that of H^+ with negligible concentration[75]. The charge/discharge process through O^{2-} intercalation/de-intercalation is advantageous since it delivers two charges, rather than the typical single charge carriers. Therefore, a notable enhancement in the specific capacitance is expected[76]. The free O^{2-} intercalates into the vacancy sites, which is then accompanied by proton transfer to the electrolyte hydroxide ions yielding water as a product[74]. At a very low OH^- concentration (0.1 M), shown in **Figure 4**a, the peak associated with the $Mn^{3+} \rightarrow Mn^{4+}$ reaction is significantly decreased confirming the significant role of OH^- concentration in O^{2-} anion intercalation.

Owing to the large ionic radius of O^{2-}, the intercalation is anticipated to be kinetically slow and hence diffusion-controlled. This is supported by voltammograms obtained at scan rates of 20, 40, and 80 mV s^{-1} (**Figure 4**b**)**. The increase in the scan rate revealed to shift the anodic peaks into higher potential that can be attributed to the sluggish kinetics of O^{2-} intercalation within the insufficient scanning time. In contrast, for the cathodic cycle, increasing scan rate resulted in an insignificant shift in the cathodic peak potentials. This is owing to the fact that, during the cathodic cycle, the restoration of the vacancies occurs by breaking the chemical bonds between the intercalated O^{2-} and coordinated Mn atoms. Therefore, de-intercalation of the as-released O^{2-} would not affect the peak potentials by raising the scan rate.

To further confirm that O^{2-} intercalation has substantial contribution in energy storage performance of the $Mn_{1-x-y}(Ce_xLa_y)O_{2-\delta}$, **Figure 4**c shows voltammograms of $Mn_{1-x-y}(Ce_xLa_y)O_{2-\delta}$ obtained in basic electrolytes with Li^+, Na^+, K^+ charge carriers and neutral electrolyte of 2M Na_2SO_4. The measurement of voltammogram areas (**Figure 4**d) revealed that the capacitances obtained in basic electrolytes exhibited ~15% increase comparing to the one obtained in neutral electrolyte. Further, the type of charge carriers in basic electrolytes showed no significant impact on the capacitance.

Another critical factor in controlling the rate of intercalation/de-intercalation of O^{2-} is the density of Mn cations, with lower oxidation states, and probably oxygen vacancies, which act as active sites to entrap the

O^{2-} species. The presence of these active sites has shown to change the electronic conductivity of the $Mn_{1-x-y}(Ce_xLa_y)O_{2-\delta}$ by realignment of the band positions, possibly through an introduction of midgap states [77]. Additionally, the formation of midgap states can also be attributed to the presence of La^{3+} and Ce^{3+} ions. The Tauc plot shown in **Figure 1**d unveiled such an alteration, relative to the pristine MnO_{2-x}. Furthermore, the multivalence charge transfer (MVCT) between the RE and Mn ions significantly impacts the electrochemical performance through improving the electrical conductivity[50,77,78]. Another reason for improved electrochemical performance of the $Mn_{1-x-y}(Ce_xLa_y)O_{2-\delta}$ is the formation of tensile distortion, owing to the presence of RE ions at the interstitial sites of the lattice, thus enabling ion transport by newly established atomic channels[12,79].

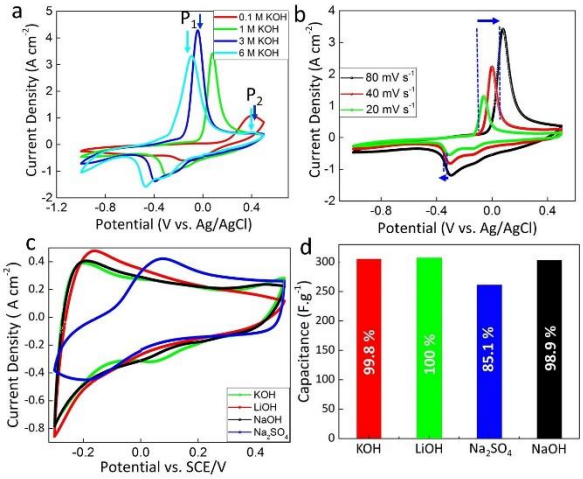

Figure 4. Effect of electrolyte concentration on redox reactions and intercalation mechanism of ions, using an electrode made of #IV ultrathin film; a) CVs at the scan rate of 80 $mV.s^{-1}$ in aqueous KOH electrolytes of varying concentration, b) CVs at 1 M KOH electrolyte at different scan rates, c) CVs at electrolyte with charge carrier cations of 2 M Li^+, Na^+, K^+, and neutral electrolyte of SO_4^{2-} (using Na_2SO_4), and d) corresponding gravimetric capacitance.

Impact of RECs insertion on cyclic stability. Comparative analyses were carried out to explore the chemical alterations of MnO_{2-x} and $Mn_{1-x-y}(Ce_xLa_y)O_{2-\delta}$ electrode during charge/discharge cycling. Therefore, the variations of defect concentrations, as a reflection of Mn oxidation states, before and after charge/discharge of 1st and 16000th cycles for pristine MnO_{2-x} and $Mn_{1-x-y}(Ce_xLa_y)O_{2-\delta}$ were examined using XPS analysis, the results of which are shown in **Figure 5**. **Figure 5**a and b show the XPS spectra for Mn $2p_{3/2}$ orbital of pristine MnO_{2-x} and $Mn_{1-x-y}(Ce_xLa_y)O_{2-\delta}$. The spectra are deconvoluted into four distinctive multiplets using Gaussian fitting technique. The multiplets positioned at 641.1, 642.2, and 643.5 eV are assigned to Mn^{2+}, Mn^{3+}, and Mn^{4+}, respectively.

The atomic concentrations of the Mn oxidation states for as-synthesised MnO_{2-x}, fully-discharged MnO_{2-x} after a cycle, and fully-discharged MnO_{2-x} after 16000 cycles are plotted in **Figure 5**c. The low Mn oxidation states (Mn^{2+} and Mn^{3+}), which are counted as active sites, where O^{2-} anions can be inserted, are crucial to enhance the capacitance. In contrast, the Mn^{4+}, which is obtained after fully-discharge process, is practically inactive for energy storage performance. In the present work, MnO_{2-x} exhibits a typical behaviour, similar to other TMOs reported previously, in that Mn^{2+} and Mn^{3+} concentrations decrease with cycling, while Mn^{4+} concentration shows an increasing trend. Therefore, the capacitance retention is expected to decrease over the cycling, which is well in consistent with 40% capacitance reduction after 16000 cycles.

Nonetheless, the XPS results for $Mn_{1-x-y}(Ce_xLa_y)O_{2-\delta}$ sample, as shown in **Figure 5**d, revealed an unprecedented behaviour, where the atomic concentrations of Mn^{2+} and Mn^{3+} increased during discharge process after 16000 cycles. This is accompanied by the decrease of Mn^{4+} from 29.3 at% to 22 at%. These results rationalise the outstanding capacitance retention of $Mn_{1-x-y}(Ce_xLa_y)O_{2-\delta}$ yielding an insignificant capacitance reduction of ~10% after 16000 cycles.

A more comprehensive investigation was carried out by comparative study on Mn concentrations at charge and discharge process. For the MnO_{2-x} sample, the initial concentrations were measured to be 21.3, 56.5, and 22.2 at% for Mn^{2+}, Mn^{3+}, and Mn^{4+}, respectively (**Figure 5**a). The 1st cycle of charge resulted in oxidation of Mn^{2+} and Mn^{3+} toward Mn^{4+}. Therefore, the concentration of Mn^{2+} and Mn^{3+} decreased to 19.5 at% and 48.3 at%, while Mn^{4+} concentration increased by 10% to 32 at% (**Figure 5**e). During the following discharge process, however, an incomplete rehabilitation of Mn oxidation states occurred that caused the reduction of Mn^{2+} and Mn^{3+} concentrations, relative to the as-synthesised sample, which led to evolution of Mn^{4+}. The resultant concentrations of Mn^{2+}, Mn^{3+}, and Mn^{4+} after fist cycle of discharge were measured to be 21.1 %, 51.4 %, 26.7%, respectively (**Figure 5**f). The constant reduction of Mn^{2+} and Mn^{3+} during 16000 charge/discharge cycles was observed, as shown in **Figure 5**f.

Figure 5b shows as-synthesised $Mn_{1-x-y}(Ce_xLa_y)O_{2-\delta}$ possessing high densities of Mn with low oxidation states, *i.e.*, Mn^{2+} (16.3 at%) and Mn^{3+} (54.4 at%), and only 29.3 at% of Mn^{4+}. During the 1st cycle of charge, Mn^{2+} and Mn^{3+} are oxidised to Mn^{4+} leading to a drop in the Mn^{2+}/Mn^{3+} concentrations by respective ~1% and 7%, while Mn^{4+} concentration increased to 36.5% (**Figure 5**g). Upon discharge (**Figure 5**h), not only were the Mn^{2+} and Mn^{3+} concentrations fully reversed, but also new Mn^{2+} states were generated. The concentrations of Mn^{2+}, Mn^{3+}, and Mn^{4+} were measured to be 17.9 %, 49.6 %, 25.5%, respectively. The similar trend was observed after 16000 cycles.

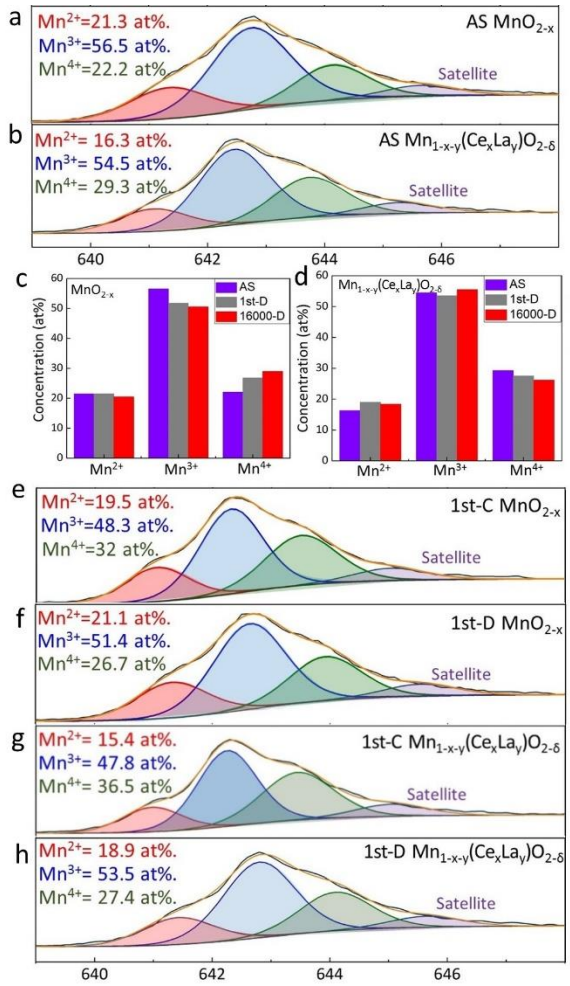

Figure 5. XPS spectra associated with the Mn $2p_{3/2}$ of a) pristine MnO_{2-x}, b) $Mn_{1-x-y}(Ce_xLa_y)O_{2-\delta}$. Alteration of Mn oxidation state, discharge (D) of 1st and 16000th cycles for c) pristine MnO_{2-x}, and d) $Mn_{1-x-y}(Ce_xLa_y)O_{2-\delta}$, (AS stands for as-synthesised). XPS spectra associated with the Mn $2p_{3/2}$ of pristine MnO_{2-x} showing the concentration of Mn^{2+}, Mn^{3+}, Mn^{4+} during 1st cycle's e) charge (C), and f) discharge (D). XPS spectra associated with the Mn $2p_{3/2}$ of $Mn_{1-x-y}(Ce_xLa_y)O_{2-\delta}$ showing the concentration of Mn^{2+}, Mn^{3+}, Mn^{4+} during 1st cycle's g) charge (C), and h) discharge (D).

The microstructure of the pristine MnO_{2-x} and $Mn_{1-x-y}(Ce_xLa_y)O_{2-\delta}$ were examined after 2500 and 16000 cycles, respectively, and the corresponding SEM images are shown in **Figure 5**6a-d. It clearly reveals the trend in that nanoflakes in the as-synthesised pristine MnO_{2-x} transform to nanowires after 2500 cycling test while the microstructure of $Mn_{1-x-y}(Ce_xLa_y)O_{2-\delta}$ remained unchanged even after 16000 cycles. These results confirm that the REC interstitials play a critical role in retaining the microstructure and hence the energy storage performance[79,80].

In summary, morphology, phase stability, and conductivity are three key factors induced by REC insertion resulting in achieving promising pseudocapacitor electrodes with significantly enhanced performance stability.

Electrochemical performance of flexible, transparent, symmetric pseudocapacitance device. Capacitance values can significantly vary in different experimental setups even with identical materials[81,82]. The electrochemical performance of the $Mn_{1-x-y}(Ce_xLa_y)O_{2-\delta}$ ultrathin film with a thickness of 46 nm (#IV) was studied by synthesis of a flexible symmetric pseudocapacitance device. The rationale to select sample #IV was for a fully combined study of transparency and areal, gravimetric, and volumetric capacitances. **Figure 6**a shows voltammograms obtained in a symmetric two-electrode ($Mn_{1-x-y}(Ce_xLa_y)O_{2-\delta}$ film coated on FTO) configuration system in a 2 M KOH aqueous solution at scan rates ranging from 50 to 1000 $mV{\cdot}s^{-1}$ within the potential window of −0.3 and +0.5 V vs SCE. The clear rectangular shape of the voltammogram is an indication of the EDL and pseudocapacitance behaviour. The gravimetric and areal capacitances of the electrode as a function of scan rate were plotted, as shown in **Figure 6**b. Both specific capacitances decrease by increasing the scan rate, similar to the three-electrode configuration system. According to the theory reported in the literature[81], the specific capacitance obtained from the three-electrode system is calculated to be ca. quadruple that from the symmetric two-electrode system even with totally identical materials[82]. For instance, comparing the gravimetric capacitance (142 $F.g^{-1}$) obtained from the two-electrode aqueous setup at a scan rate of 5 mV s^{-1} (**Figure 6**b) with the one (489 $F.g^{-1}$) obtained from the three-electrode configuration (for #IV) under the same condition (**Figure S4**h, Supporting Information) indicates that in our work $C_{three\text{-}electrode}=3.4\times C_{two\text{-}electrode}$, showing that the two-electrode configuration is very close to what is expected based on theoretical calculations.

The quasi-triangle shape of the GCD profiles at various current densities are also shown in **Figure 6**7a, Supporting Information. The areal and gravimetric capacitances in **Figure 6**c are in accordance with those obtained from the cyclic voltammetry method (**Figure 5**b). Further comparison between the gravimetric capacitance values resulted from two-electrode GCD test (132 $F.g^{-1}$) at a specific current of 10 $A.g^{-1}$ (**Figure 6**c) with the one (466 $F.g^{-1}$) obtained under the three-electrode setup (for #IV at **Figure S4**i, Supporting Information) shows that $C_{three\text{-}electrode}=3.5C_{two\text{-}electrode}$, which is consistent with the CV comparison and also close to the theoretical value. The cycling stability of the two-electrode system was evaluated using the GCD method (**Figure 6**d). The results show high capacitance retention of ~82 % after a large number of cycles (16000) at a current density of 10 $A{\cdot}g^{-1}$.

The two-electrode configuration system was further analysed using a device with a solid-state electrolyte (a gel mixed of LiCl, Polyvinylalcohol (PVA), and H_2O), which are superior, in terms of safety, compared to conventional liquid electrolytes[83]. **Figure S4**b, Supporting Information, shows the resultant cyclic voltammograms at scan rates in the range of 50-100

$mV.s^{-1}$ and in the potential window from -0.3 to +0.5 V vs SCE.

The small deviation from the ideal-rectangular shape and lower current density can be attributed to the larger electrical resistance resulting from the slower electron transfer rate within the solid electrolyte. This is shown in **Figure 6**e, where the gravimetric and areal capacitances of the symmetric two-electrode device, as a function of scan rate in a solid electrolyte, experience a slight decrease compared with those of obtained from the similar system but in aqueous electrolyte, suggesting great applicability of the $Mn_{1-x-y}(Ce_xLa_y)O_{2-\delta}$ ultrathin films to use as a promising electrode in flexible and transparent pseudocapacitance devices.

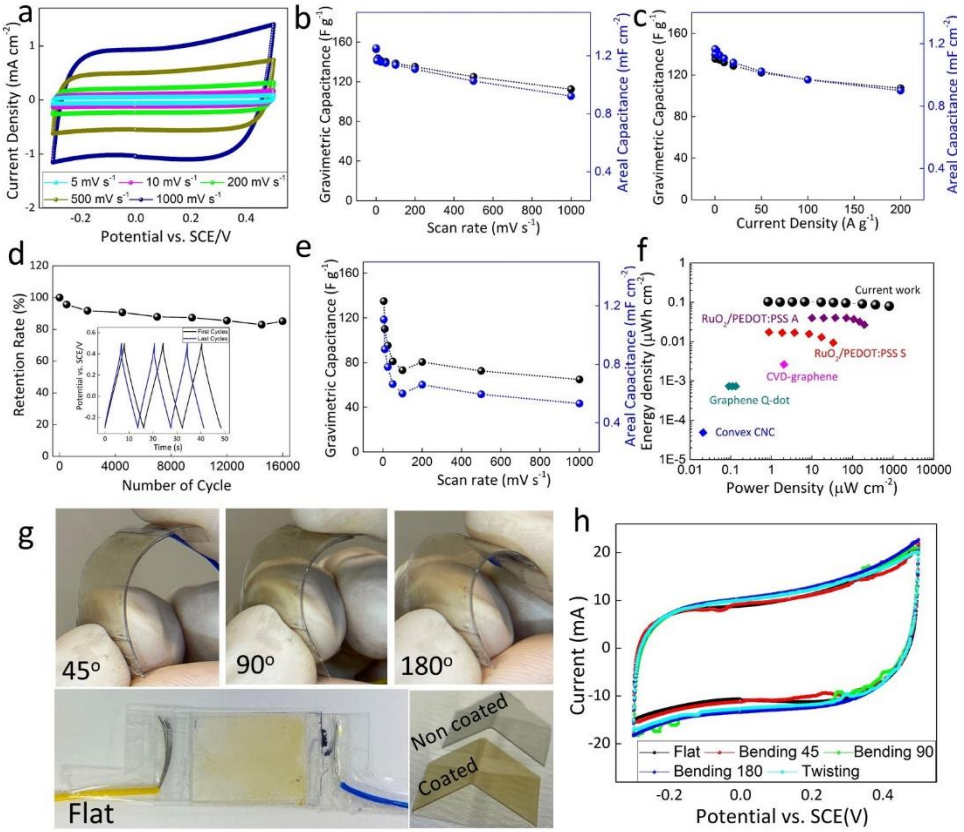

Figure 6. The results of the symmetric two-electrode ($Mn_{1-x-y}(Ce_xLa_y)O_{2-\delta}$ film coated on FTO) cell in 2 M KOH aqueous solution and room temperature: a) CVs at different scan rates, b) gravimetric and areal capacitances as a function of scan rate, c) gravimetric and areal capacitances as a function of current density, and d) stability performance at current density of 10 $A.g^{-1}$. The results of $Mn_{1-x-y}(Ce_xLa_y)O_{2-\delta}$ ultrathin-film (deposited on FTO substrate) solid-state symmetric device: e) areal and gravimetric capacitances as a function of scan rate, and f) Ragone plot along with values for other devices developed in the literature. The results of the flexible solid-state symmetric two-electrode cell (the films deposited on ITO coated flexible PET); g) photographs of the pseudocapacitor, h) CVs after twisting and bending.

The power and energy densities of the device were also measured and comparatively studied with the outstanding values for flexible ultrathin films reported recently, as shown in **Figure 6**f. Both the power and energy densities exhibited high values compared with those reported from benchmark pseudocapacitor devices (either symmetric or asymmetric) including RuO_2/PEDOT:PSS[4], carbon nanocap (CNC)[31], pristine graphene[84], and reduced multilayer graphene oxide (RMGO)[84].

The flexible and transparent device was fabricated by controllable deposition of the $Mn_{1-x-y}(Ce_xLa_y)O_{2-\delta}$ on an ITO-coated flexible PET substrate and applying the solid electrolyte, as shown in **Figure 6**g. The energy and power densities of the ultrathin film-based flexible device were measured using CV analysis in a wide range of scan rates between 50 and 1000 $mV\ s^{-1}$. The results are shown in **Figure S6**c and d, Supporting Information. As a flexible and portable capacitor device, the variations of the electrochemical performance upon twisting and bending of electrodes at different angles of 45°, 90°, and 180° (**Figure 6**g) was explored. **Figure 6**h shows that the cyclic voltammogram area remains unaffected during the twisting and bending, which illustrates the mechanical stability of the device. Furthermore, the inset of **Figure 6**g and Supplementary **Video S1** and **S2**, Supporting Information, depict a full comparative analysis of the coated and uncoated substrates. These experiments revealed high homogeneity, transparency, flexibility, and remarkable adherence of the film even after complete folding of the substrate. Such excellent

mechanical flexibility and stability of the device as well as the strongly adherent film on the substrate, even after vigorous bending and twisting, unveils great potential for the use of these advanced functional materials for state-of-the-art flexible and transparent pseudocapacitance applications.

3. Conclusion

The present work demonstrated fabrication of flexible, transparent $Mn_{1-x-y}(Ce_xLa_y)O_{2-\delta}$ pseudocapacitor devices using a spent-batteries derived precursor. A representative ultrathin film with high transmittance of 86% exhibited an excellent areal and gravimetric capacitances of 3.4 $mF{\cdot}cm^{-2}$ and 720 $F{\cdot}g^{-1}$. The excellent electrochemical performance was mainly ascribed to the anionic intercalation/de-intercalation of O^{2-} into the atomic tunnels of $Mn_{1-x-y}(Ce_xLa_y)O_{2-\delta}$ crystal structure, which is first to report for an oxide-based pseudocapactior. Further, the $Mn_{1-x-y}(Ce_xLa_y)O_{2-\delta}$ yielded outstanding capacitance retention of ~90% after 16,000 cycles, which can be ascribed to the rapid redox reactions between multivalence oxidation states of extrinsic Ce^{3+}, Ce^{4+}, and La^{3+} ions at the interstitial sites and intrinsic Mn ions in $Mn_{1-x-y}(Ce_xLa_y)O_{2-\delta}$ lattice. Such rapid exchange in oxidation states resulted in an insignificant reduction of Mn cations with low oxidation states (i.e. Mn^{2+} and Mn^{3+}) during long-term cycling. Further, the electrochemical performance of a representative symmetric full-cell $Mn_{1-x-y}(Ce_xLa_y)O_{2-\delta}$ pseudocapacitor with solid-state electrolyte was tested under twisting and bending at 45°, 90° and 180°, where no significant attenuation in performance was recorded. The present work establishes a new pathway to synthesis TMO-based pseudocapacitors with engineered defects and electronic properties to obtain pseudocapacitors with desired flexibility, transparency and cycling stability suitable for size-sensitive, portable, and wearable power-integrated electronic devices.

4. Future Perspective

5. Experimental Section

A detailed description of fabrication processes, mechanisms, characterisations, computational studies, and additional analysis can be found in the Supporting Information.

Supporting Information

Supporting information is available from the Wiley Online Library or from the corresponding authors.

Acknowledgements

This work has been supported by …

Conflict of Interest

The authors declare no conflict of interest

Keywords:

References

[1] B. Xie, Y. Wang, W. Lai, W. Lin, Z. Lin, Z. Zhang, P. Zou, Y. Xu, S. Zhou, C. Yang, F. Kang, C.-P. Wong, *Nano Energy* **2016**, *26*, 276.

[2] Z. Lei, J. Zhang, L. L. Zhang, N. A. Kumar, X. S. Zhao, *Energy Environ. Sci.* **2016**, *9*, 1891.

[3] Y.-H. Liu, J.-L. Xu, X. Gao, Y.-L. Sun, J.-J. Lv, S. Shen, L.-S. Chen, S.-D. Wang, *Energy Environ. Sci.* **2017**, *10*, 2534.

[4] C. Zhang, T. M. Higgins, S.-H. Park, S. O'Brien, D. Long, J. Coleman, V. Nicolosi, *Nano Energy* **2016**, *28*, 495.

[5] J. Chen, Y. Huang, N. Zhang, H. Zou, R. Liu, C. Tao, X. Fan, Z. L. Wang, *Nat. Energy* **2016**, *1*, 16138.

[6] D. J. Lipomi, B. C.-K. Tee, M. Vosgueritchian, Z. Bao, *Adv. Mater.* **2011**, *23*, 1771.

[7] X. Y. Liu, Y. Q. Gao, G. W. Yang, *Nanoscale* **2016**, *8*, 4227.

[8] T. Chen, Y. Xue, A. K. Roy, L. Dai, *ACS Nano* **2014**, *8*, 1039.

[9] P. Xu, J. Kang, J.-B. Choi, J. Suhr, J. Yu, F. Li, J.-H. Byun, B.-S. Kim, T.-W. Chou, *ACS Nano* **2014**, *8*, 9437.

[10] S. Sollami Delekta, A. D. Smith, J. Li, M. Östling, *Nanoscale* **2017**, *9*, 6998.

[11] N. Li, G. Yang, Y. Sun, H. Song, H. Cui, G. Yang, C. Wang, *Nano Lett.* **2015**, *15*, 3195.

[12] X. Yang, W. Peng, K. Fu, L. Mao, J. Jin, S. Yang, G. Li, *Electrochim. Acta* **2020**, *340*, 135989.

[13] Y. Zhong, X. Zhang, Y. He, H. Peng, G. Wang, G. Xin, *Adv. Funct. Mater.* **2018**, *28*, 1801998.

[14] C. (John) Zhang, V. Nicolosi, *Energy Storage Mater.* **2019**, *16*, 102.

[15] C. (John) Zhang, B. Anasori, A. Seral-Ascaso, S.-H. Park, N. McEvoy, A. Shmeliov, G. S. Duesberg, J. N. Coleman, Y. Gogotsi, V. Nicolosi, *Adv. Mater.* **2017**, *29*, 1702678.

[16] X. Jiao, C. Zhang, Z. Yuan, *ACS Appl. Mater. Interfaces* **2018**, *10*, 41299.

[17] K. Devarayan, D. Lei, H.-Y. Kim, B.-S. Kim, *Chem. Eng. J.* **2015**, *273*, 603.

[18] T. Cheng, Y.-Z. Zhang, J.-D. Zhang, W.-Y. Lai, W. Huang, *J. Mater. Chem. A* **2016**, *4*, 10493.

[19] T. M. Higgins, J. N. Coleman, *ACS Appl. Mater. Interfaces* **2015**, *7*, 16495.

[20] M. A. Borysiewicz, M. Ekielski, Z. Ogorzałek, M. Wzorek, J. Kaczmarski, T. Wojciechowski, *Nanoscale* **2017**, *9*, 7577.

[21] F. Liu, X. Yang, Z. Qiao, L. Zhang, B. Cao, G. Duan, *Electrochim. Acta* **2018**, *260*, 281.

[22] X. Liu, J. Wang, G. Yang, *Chem. Eng. J.* **2018**, *347*, 101.

[23] P. Suktha, N. Phattharasupakun, M. Sawangphruk,

Sustain. Energy Fuels **2018**, *2*, 1799.
[24] L. Shen, L. Du, S. Tan, Z. Zang, C. Zhao, W. Mai, *Chem. Commun.* **2016**, *52*, 6296.
[25] A. K. Sundramoorthy, Y.-C. Wang, S. Gunasekaran, *Nano Res.* **2015**, *8*, 3430.
[26] R. Yuksel, Z. Sarioba, A. Cirpan, P. Hiralal, H. E. Unalan, *ACS Appl. Mater. Interfaces* **2014**, *6*, 15434.
[27] H. Moon, H. Lee, J. Kwon, Y. D. Suh, D. K. Kim, I. Ha, J. Yeo, S. Hong, S. H. Ko, *Sci. Rep.* **2017**, *7*, 41981.
[28] H. Sheng, X. Zhang, Y. Ma, P. Wang, J. Zhou, Q. Su, W. Lan, E. Xie, C. Zhang, *ACS Appl. Mater. Interfaces* **2019**, *11 9*, 8992.
[29] S. Kiruthika, C. Sow, G. U. Kulkarni, *Small* **2017**, *13*, 1701906.
[30] Y. Wang, W. Zhou, Q. Kang, J. Chen, Y. Li, X. Feng, D. Wang, Y. Ma, W. Huang, *ACS Appl. Mater. Interfaces* **2018**, *10*, 27001.
[31] H. Y. Jung, M. B. Karimi, M. G. Hahm, P. M. Ajayan, Y. J. Jung, *Sci. Rep.* **2012**, *2*, 773.
[32] T. Qiu, B. Luo, M. Giersig, E. M. Akinoglu, L. Hao, X. Wang, L. Shi, M. Jin, L. Zhi, *Small* **2014**, *10*, 4136.
[33] Y.-H. Liu, J.-L. Xu, S. Shen, X.-L. Cai, L.-S. Chen, S.-D. Wang, *J. Mater. Chem. A* **2017**, *5*, 9032.
[34] T. Cheng, Y.-Z. Zhang, J.-P. Yi, L. Yang, J.-D. Zhang, W.-Y. Lai, W. Huang, *J. Mater. Chem. A* **2016**, *4*, 13754.
[35] I. Nam, S. Park, G.-P. Kim, J. Park, J. Yi, *Chem. Sci.* **2013**, *4*, 1663.
[36] A. Ferris, S. Garbarino, D. Guay, D. Pech, *Adv. Mater.* **2015**, *27*, 6625.
[37] D. L. Ma, Y. Ma, Z. W. Chen, A. M. Hu, *J. Mater. Chem. A* **2017**, *5*, 20608.
[38] W. Song, J. Zhu, B. Gan, S. Zhao, H. Wang, C. Li, J. Wang, *Small* **2018**, *14*, 1702249.
[39] J. Ge, G. Cheng, L. Chen, *Nanoscale* **2011**, *3*, 3084.
[40] K. Gao, Z. Shao, X. Wu, X. Wang, Y. Zhang, W. Wang, F. Wang, *Nanoscale* **2013**, *5*, 5307.
[41] T. Chen, H. Peng, M. Durstock, L. Dai, *Sci. Rep.* **2014**, *4*, 3612.
[42] P. Kanninen, N. D. Luong, L. H. Sinh, I. V Anoshkin, A. Tsapenko, J. Seppälä, A. G. Nasibulin, T. Kallio, *Nanotechnology* **2016**, *27*, 235403.
[43] Z. Morgan Chan, D. A. Kitchaev, J. Nelson Weker, C. Schnedermann, K. Lim, G. Ceder, W. Tumas, M. F. Toney, D. G. Nocera, *Proc. Natl. Acad. Sci.* **2018**, *115*, E5261 LP.
[44] L. Yang, S. Cheng, J. Wang, X. Ji, Y. Jiang, M. Yao, P. Wu, M. Wang, J. Zhou, M. Liu, *Nano Energy* **2016**, *30*, 293.
[45] M. Sun, B. Lan, T. Lin, G. Cheng, F. Ye, L. Yu, X. Cheng, X. Zheng, *CrystEngComm* **2013**, *15*, 7010.
[46] T. Gao, H. Fjellvåg, P. Norby, *Anal. Chim. Acta* **2009**, *648*, 235.
[47] A. Ramírez, P. Hillebrand, D. Stellmach, M. M. May, P. Bogdanoff, S. Fiechter, *J. Phys. Chem. C* **2014**, *118*, 14073.
[48] M. Huang, F. Li, F. Dong, Y. X. Zhang, L. L. Zhang, *J. Mater. Chem. A* **2015**, *3*, 21380.
[49] Z. Y. Leong, H. Y. Yang, *ACS Appl. Mater. Interfaces* **2019**, *11*, 13176.
[50] K. Chen, W. Pan, D. Xue, *J. Phys. Chem. C* **2016**, *120*, 20077.
[51] Y. Yuan, S. M. Wood, K. He, W. Yao, D. Tompsett, J. Lu, A. Nie, M. S. Islam, R. Shahbazian-Yassar, *ACS Nano* **2016**, *10*, 539.
[52] S. Devaraj, N. Munichandraiah, *J. Phys. Chem. C* **2008**, *112*, 4406.
[53] D. A. Tompsett, S. C. Parker, M. S. Islam, *J. Am. Chem. Soc.* **2014**, *136*, 1418.
[54] L. Wang, Y. Yu, H. He, Y. Zhang, X. Qin, B. Wang, *Sci. Rep.* **2017**, *7*, 12845.
[55] W. Zhang, Z. Yang, Y. Liu, S. Tang, X. Han, M. Chen, *J. Cryst. Growth* **2004**, *263*, 394.
[56] O. Ghodbane, F. Ataherian, N.-L. Wu, F. Favier, *J. Power Sources* **2012**, *206*, 454.
[57] Z. Hu, X. Xiao, C. Chen, T. Li, L. Huang, C. Zhang, J. Su, L. Miao, J. Jiang, Y. Zhang, J. Zhou, *Nano Energy* **2015**, *11*, 226.
[58] B.-A. Mei, J. Lau, T. Lin, S. H. Tolbert, B. S. Dunn, L. Pilon, *J. Phys. Chem. C* **2018**, *122*, 24499.
[59] T. Gu, B. Wei, *Nanoscale* **2015**, *7*, 11626.
[60] J. Creus, F. Brezault, C. Rebere, M. Gadouleau, *Surf. Coatings Technol.* **2006**, *200*, 4636.
[61] A. Buffa, D. Mandler, *Electrochim. Acta* **2019**, *318*, 496.
[62] P. J. King, T. M. Higgins, S. De, N. Nicoloso, J. N. Coleman, *ACS Nano* **2012**, *6*, 1732.
[63] A. Ponzoni, *Appl. Phys. Lett.* **2019**, *114*, 153105.
[64] P. Salles, E. Quain, N. Kurra, A. Sarycheva, Y. Gogotsi, *Small* **2018**, *14*, 1802864.
[65] E. Jokar, S. Shahrokhian, A. I. zad, E. Asadian, H. Hosseini, *J. Energy Storage* **2018**, *17*, 465.
[66] B. Ruzicka, L. Degiorgi, R. Gaal, L. Thien-Nga, R. Bacsa, J. Salvetat, L. Forró, *Phys. Rev. B - Condens. Matter Mater. Phys.* **2000**, *61*, R2468.
[67] E. M. Doherty, S. De, P. E. Lyons, A. Shmeliov, P. N. Nirmalraj, V. Scardaci, J. Joimel, W. J. Blau, J. J. Boland, J. N. Coleman, *Carbon N. Y.* **2009**, *47*, 2466.
[68] S. De, P. J. King, M. Lotya, A. O'Neill, E. M. Doherty, Y. Hernandez, G. S. Duesberg, J. N. Coleman, *Small* **2010**, *6*, 458.
[69] M. Toupin, T. Brousse, D. Bélanger, *Chem. Mater.* **2004**, *16*, 3184.
[70] X. Lang, A. Hirata, T. Fujita, M. Chen, *Nat. Nanotechnol.* **2011**, *6*, 232.
[71] C.-C. Hu, K.-H. Chang, M.-C. Lin, Y.-T. Wu, *Nano Lett.* **2006**, *6*, 2690.
[72] H. Lindström, S. Södergren, A. Solbrand, H. Rensmo, J. Hjelm, A. Hagfeldt, S.-E. Lindquist, *J. Phys. Chem. B* **1997**, *101*, 7717.
[73] V. Augustyn, J. Come, M. A. Lowe, J. W. Kim, P.-L. Taberna, S. H. Tolbert, H. D. Abruña, P. Simon, B. Dunn, *Nat. Mater.* **2013**, *12*, 518.
[74] J. T. Mefford, W. G. Hardin, S. Dai, K. P. Johnston, K. J. Stevenson, *Nat. Mater.* **2014**, *13*, 726.
[75] H. P. Boehm, *Discuss. Faraday Soc.* **1971**, *52*, 264.
[76] Y. Liu, S. P. Jiang, Z. Shao, *Mater. Today Adv.* **2020**, *7*, 100072.
[77] J.-L. Shi, D.-D. Xiao, M. Ge, X. Yu, Y. Chu, X. Huang, X.-D. Zhang, Y.-X. Yin, X.-Q. Yang, Y.-G. Guo, L. Gu, L.-J. Wan, *Adv. Mater.* **2018**, *30*, 1705575.
[78] D. Chen, D. Ding, X. Li, G. H. Waller, X. Xiong, M. A. El-Sayed, M. Liu, *Chem. Mater.* **2015**, *27*, 6608.
[79] R. Dong, Q. Ye, L. Kuang, X. Lu, Y. Zhang, X. Zhang, G. Tan, Y. Wen, F. Wang, *ACS Appl. Mater. Interfaces* **2013**, *5*, 9508.
[80] Z. Wang, Q. Qin, W. Xu, J. Yan, Y. Wu, *ACS Appl.*

Mater. Interfaces **2016**, *8*, 18078.
[81] S. Zhang, N. Pan, *Adv. Energy Mater.* **2015**, *5*, 1401401.
[82] V. Khomenko, E. Frackowiak, F. Béguin, *Electrochim. Acta* **2005**, *50*, 2499.
[83] A. Varzi, R. Raccichini, S. Passerini, B. Scrosati, *J. Mater. Chem. A* **2016**, *4*, 17251.
[84] J. J. Yoo, K. Balakrishnan, J. Huang, V. Meunier, B. G. Sumpter, A. Srivastava, M. Conway, A. L. Mohana Reddy, J. Yu, R. Vajtai, P. M. Ajayan, *Nano Lett.* **2011**, *11*, 1423.

Table of Content: